Desalination and Water Treatment
www.deswater.com

doi: 10.5004/dwt.2020.25990

197 (2020) 200–212
September

Visible light-driven Ag_2S–PbS photocatalyst for photocatalytic degradation of phenazopyridine in aqueous solution

Sakineh Salmanderis[a,b], Alireza Nezamzadeh-Ejhieh[a,b,c,*]

[a]*Department of Chemistry, Shahreza Branch, Islamic Azad University, P.O. Box: 311-86145, Shahreza, Isfahan, Iran, Tel. +98 31-53292500; emails: arnezamzadeh@iaush.ac.ir (A. Nezamzadeh-Ejhieh), s.salmanderis@gmail.com (S. Salmanderis)*
[b]*Young Researchers and Elite Club, Shahreza Branch, Islamic Azad University, Shahreza, Iran*
[c]*Razi Chemistry Research Center (RCRC), Shahreza Branch, Islamic Azad University, Isfahan, Iran*

Received 5 August 2019; Accepted 16 April 2020

ABSTRACT

For increasing the photocatalytic activity of PbS and Ag_2S nanoparticles, their coupled system was constructed mechanically and characterized by X-ray diffraction, scanning electron microscopy, diffuse reflectance spectroscopy, photoluminescence (PL) and Fourier-transform infrared spectroscopy techniques. Then, the photocatalytic activity of the single and coupled systems was evaluated in the degradation of phenazopyridine in aqueous solution. The results showed a synergistic photocatalytic effect for the coupled system with respect to the single systems. PL results showed a lower PL intensity for the coupled system, confirming lower recombination of the photogenerated electron/hole pairs. The coupled system showed also a higher photocatalytic activity of the coupled system. The coupled Ag_2S/PbS catalyst with a mole ratio of 2:1 showed the best photocatalytic activity for 75 min. This catalyst showed also the lowest PL intensity with respect to the other coupled systems with different mole ratios. Based on the chemical oxygen demand results a rate constant of 1.41×10^{-3} was obtained for the mineralization of PhP solution for 50 min irradiation time, while the value of 1.80×10^{-3} min^{-1} was obtained for its degradation extent at the same conditions.

Keywords: Phenazopyridine; Semiconducting based photocatalysis; Coupled semiconductors; Visible light-driven photocatalyst; Hinshelwood kinetic model

1. Introduction

Growing development in different industries such as dyes and pharmaceutical facilities etc. have caused an increased discharging of different organic pollutants into the environment. This has led to the degradation of the environment due to the excessive release of such toxic chemicals. One of these technologies is the pharmaceutical industries. The wide use of drugs polluted the aquatic environments by discharging of the hospital and urban effluents as wastewater and caused a major problem for body life [1–4]. Phenazopyridine (PZP), as a local anesthetic, is commonly used to relieve symptoms caused by irritation of the urinary tract such as pain, burning, and the feeling of needing to urinate urgently or frequently. As a dye, it acts as a painkiller to soothe the lining of the urinary tract. Its applications have limited due to its problems such as toxicity (primarily blood disorders) and potential carcinogenicity. Its important side effects are pale skin, fever, confusion or weakness, jaundice (yellowing of your skin or eyes), swelling, weight gain, feeling short of breath; blue or purple coloring in our skin, etc [5]. Due to these side effects, it was subjected as a typical pharmaceutical pollutant in the present work to be degraded by the heterogeneous photocatalysis technique.

In semiconductor-based photodegradation technology, four reactive species including the photogenerated electrons and hole (e/h) pairs, superoxide and hydroxyl radicals are

* Corresponding author.

responsible for the degradation of the different pollutants molecules present in the investigated aquatic media. The final goal of this technology is mineralizing of organic pollutants into carbon dioxide and water molecules etc. The mechanism of the process has been discussed in detail in the literature [6–18]. The high efficiency of such technology can be limited by the fast e/h recombination process. To diminish this drawback or the fast separation of e/h pairs, different strategies of coupling of semiconductors, doping, supporting and use of nanoparticles (NPs) have been used [19–28].

In this work, to enhance the photocatalytic activity of PbS and Ag_2S semiconductors, we used the coupling and nano-dimension strategies. When the nano-particles of such semiconductors use, the path length for the migration of the photo-induced electrons and holes rapidly decreases. This causes the rapid migration of e/h pairs to the surface of the catalyst and reacts with O_2, H_2O and organic pollutants present in the contacted solution before they can recombine with together.

PbS is an active semiconductor with a narrow bandgap of about 0.41 eV. In a precise description, it is sensitive to radiation at wavelength range approximately from 1 to 2.5 μm (correspond to a near infra-red portion of the spectrum). PbS with a high dielectric constant and high carrier mobility has different applications in fiber optics, infrared detectors, telecommunications, lasers, optical switches, photovoltaic solar cells, biological systems, storage batteries and photography [29–31]. Ag_2S, as a member of I-VI semiconductor materials, has a bandgap between 1 to 2 eV with a monoclinic crystal structure. It has different applications in photo-conducting cells, infrared detectors, and solar selective coating. Thus, Ag_2S has used as a promising material for the conversion of solar energy into electricity [32].

The ability of a series of Ag_2S–Ag_2CO_3 composites with different amounts of Ag_2S has evaluated in the photodegradation of methyl orange, phenol, and bisphenol A. An excellent photocatalytic performance has obtained over the composite with respect to Ag_2S and Ag_2CO_3 due to the formation of Ag_2S/Ag_2CO_3 well-contacted interface and unique electron structures [33]. The boosted effect of Ag_2S quantum dots with the hexagonal SnS_2 has also studied in the photodegradation of methyl orange and Cr(IV) removal. The photogenerated holes and superoxide radicals showed a major role in MO and Cr(IV) removal [34]. In another work, the enhanced photocatalytic activity of rGO-modified Ag_2S NPs/g-C_3N_4 nanosheets has studied towards RhB [35].

The flower-like MoS_2/Ag_2S/Ag *Z*-scheme photocatalysts have constructed and the increased activity has evaluated towards congo red, tetracycline hydrochloride and disinfection for *Pseudomonas aeruginosa*. In this system, Ag acted as an electron mediator and enhanced the rate of electron transmission and the separation efficiency of photogenerated charge carriers [36]. An Ag_2S-sensitized NiO–ZnO heterostructure has used in the photodegradation of RhB with enhanced visible-light activity and electrochemical sensing towards acetone. The high sensitivity of 4.0764 μA mmol L^{-1} cm^{-2} with a low detection limit of 0.06 mmol L^{-1} has obtained for the detection of acetone [37]. In another work, *p*-xylene and chlorophenol have been degraded by TiO_2/Ag_2S nanocomposite with a boosted photocatalytic activity with respect to the single systems [38]. The photocatalytic performance of a ternary Ag_2S/ZnO/ZnS nanocomposite with a high visible light response has evaluated towards water photolysis and hydrogen production [39]. Decorated TiO_2 hierarchical spheres with Ag_2S NPs showed an enhanced photocatalytic performance towards the hydrogen production (with a rate constant of 707.6 μmol h^{-1} g^{-1}) and degradation of methyl orange (with a rate constant of 0.018 min^{-1}) [40]. Other works reported the high efficiency of supported Ag_2S or PbS onto supports, or their coupled and doped systems with other semiconducting materials in different processes such as photodegradation, H_2-production, photo-electrochemistry, and disinfection, etc [41–50].

In this work, a nanocomposite of PbS–Ag_2S was synthesized by hand mixing of the as-synthesized PbS and Ag_2S NPs and characterized by different techniques. The synergistic photocatalytic activity of the composite with respect to PbS and Ag_2S NPs alone was studied in the photodegradation of PZP as a typical pharmaceutical pollutant. The photodegradation experiments were focused on the kinetic aspects of the process.

2. Experimental setup

2.1. Materials and preparations

Silver nitrate, sodium sulfide, lead nitrate, and other analytical grade chemicals were purchased from Sigma-Aldrich Company and used for preparing aquatic solutions in distilled water. Phenazopyridine ($C_{11}H_{11}N_5$·MW: 213.24) was used as a pharmaceutical tablet (100 mg, Shahrdaro Co., Iran). A PZP tablet with a weight of 175 mg was thoroughly hand mixed in an agate mortar. Aliquot 17.5 mg of the powder was dissolved in water and then filtered into a 100 mL volumetric flask and reached the mark. The concentration of PZP in this solution was 100 mg L^{-1}.

2.2. Synthesis of the nano-materials

A 0.033 g weighted $Pb(NO_3)_2$ was added to water and stirred for 30 min to complete dissolution and diluted to the mark in a 100 mL volumetric flask (solution A). A 0.024 g portion of Na_2S was also dissolved in 100 mL distilled water completely (solution B). Solution B was added to solution A under vigorous stirring and pH reached to 9 by adding 0.2 M NaOH solution and stirring process was continued for 2 h. After centrifugation (rpm > 13,000) and many times washing, the resulted lead sulfide NPs were dried in a heating oven at 70°C and a dark gray solid was stored for next uses [51].

To synthesis Ag_2S NPs, 1.02 g of $AgNO_3$ (in 100 mL water), and 0.504 of Na_2S·$5H_2O$ solution (in 100 mL water) was completely dissolved and the sulfide solution was added dropwise into the silver solution with sonication at room temperature for 30 min (frequency, 1 kHz, amplitude: 100%, 230 V AC). Finally, the suspension was vigorously stirred for about 6 h. After centrifugation and many times washing with acetone and distilled water, it was dried under vacuum at 80°C and the resulted black Ag_2S powder NPs were obtained [52].

For the preparation of PbS–Ag_2S coupled system, the adequate weighted amount of each ingredient was thoroughly

hand mixed in an agate mortar for 10 min. The resulted in homogenous powder was used for the next studies.

2.3. Characterization methods

Phase identifications of the as-synthesized catalysts were studied by X-ray diffraction (XRD) (*X'*Pertpro, with Ni-filtered and Cu-Kα radiation at 1.5406 Å, *V*: 40 kV, *i*: 30 mA; Netherland). The surface morphology of the as-synthesized composite was studied by a scanning electron microscopy (SEM) instrument (model: TESCAN CO., Czech Republic). The UV-Vis diffuse reflectance spectroscopy (DRS) of the samples was studied by a UV-Vis spectrophotometer equipped with an optics integrating sphere and a diffuse reflectance accessory (JASCO V670, using $BasO_4$ as the reference material). A centrifuge (Sigma, 2–16P, Germany) instrument was used for the separation of nanoparticles from the suspensions. A photoluminescence (PL) spectrophotometer (PerkinElmer S45, U.K.) was used for recording PL spectra. The surface area was measured by the BELsorp-mini II instrument (MicrotracBEL Corp. Co., Japan). A pH/*p*-ion meter (JENWAY model 3505) was used for recording solutions' pH.

2.4. Photodegradation experiments

In a typical PhP photo-degradation process, a suspension of 0.5 g L^{-1} of the CdS–Ag_2S catalyst in 5 mg L^{-1} PhP solution at pH 5 was irradiated by a 100 W tungsten lamp (Osram electric Co., Iran that positioned 15 cm above the reaction cell) in a common 25 mL beaker. The magnetic stirring (200 rpm) of the suspension was done to achieve a homogeneous suspension to have repeatable experiments. At definite times, the withdrawn sample was centrifuged and the absorbance of the cleaning solution (*A*) was recorded at λ_{max} 423 nm for PZP. The recorded absorbance was compared with that of blank PZP solution (A_0) for the estimation of C/C_0 values because the absorbance corresponds to the concentration of PZP (C_0 and *C*, the initial and final concentrations, respectively) based on the Beer–Lambert law. The recorded absorbance values were also used for the calculation of the degradation efficiency (DE) of the process by using the Eq. (1) [53].

$$\text{DE \%} = \left[\left(1 - \frac{A}{A_0}\right)\right] \times 100 \quad (1)$$

3. Results and discussion

3.1. Characterization studies

3.1.1. XRD patterns

Fig. 1 shows the XRD patterns obtained for the as-synthesized PbS NPs, Ag_2S NPs and the resulted Ag_2S–PbS coupled system. All patterns were compared with the standard patterns of Ag_2S and PbS crystallite phases. This comparison confirmed that peak positions of the pattern of Ag_2S agree with the monoclinic Ag_2S crystallite phase according to JCPDS No. 14-0072. Also, based on literature [54,55], typical XRD peaks of monoclinic Ag_2S should be appeared at 2θ values of 22.5° (–101), 26° (012), 29° (111), 31.7° (–112), 33.8° (022), 34.7° (120), 37° (112), 37.9° (–103), 41° (031), 43.5° (103), 46.5° (123), 49° (–212), 53.4° (–213), 58.5° (–223), 63.8° (–134), 70° (301) and 78° (–321). Most of the mentioned peaks are present in the present XRD patterns of Ag_2S NPs and the Ag_2S–PbS coupled system. XRD peaks of FCC cubic phase of PbS should appear at 2θ values of 25.98° (111), 30.10° (200), 43.10° (220), 51.02° (311), 53.47° (222), 62.59° (400), 68.95° (331), 71.01° (420), and 79.02° (422) based on JCPDS No. 05-0592 [56]. These peaks are also present in the present XRD patterns of PbS NPs and the Ag_2S–PbS coupled system. According to the above-mentioned peaks, all XRD peaks in Fig. 1 was assigned to their corresponding *hkl* planes. It is worth mentioning that, some peaks of Ag_2S and PbS crystals were overlapped in the pattern of the nanocomposite (NC) sample.

To estimate the average crystallite size (*d*) of the coupled system the following Scherrer equation was used. In this equation, β is the excess of width line of the diffraction peak (in radian), θ is the Bragg angle (in degree) and λ is the wavelength of X-ray photons [57,58].

$$d = \frac{0.9\,\lambda}{\beta\cos\theta} \quad (2)$$

All information used for this calculation are summarized in Table SDT1 in supplementary materials. As shown, the average crystallite size of 34.3 ± 10.5, 23.1 ± 10.3 and 33.5 ± 10.5 nm were estimated for the Ag_2S NPs, PbS NPs, and Ag_2S–PbS NC, respectively.

3.1.2. Fourier-transform infrared spectroscopy of the samples

Fig. 2 shows recorded Fourier-transform infrared spectroscopy (FTIR) for the as-synthesized single semiconductors and their coupled system in this work. Generally, corresponding peaks of the adsorbed water including a broad peak at around 3,500 cm^{-1} (for its stretching mode) and other at 1,637 cm^{-1} (for its bending vibration mode) are present in all spectra. This broadband proves the moisture-absorbing capacity of the samples, especially in cases of Ag_2S and the coupled system. PbS showed absorption peaks at 602, 1,082 cm^{-1} and a weak peak at 1,388 cm^{-1}. These peaks are in agreement with the values of 608, 1,061 and 1,399 cm^{-1} that reported for PbS NPs in literature [59]. In another work [35], the absorption peaks at 616, 1,092, and 1,399 cm^{-1} have reported for heteropolar diatomic molecules of PbS.

Based on the literature, the characteristic vibration of Ag–S should appear by the appearance of absorption peaks in the range of 500–600 cm^{-1} [60]. Single PbS NPs in this work showed absorption peaks at 508 and 618 cm^{-1} that agree with the above-mentioned peaks for Ag–S bond. In the spectrum of the composite, some overlapped, broadened and shifted peaks were observed. These can be related to novel interactions of Ag–Pb, Ag–S–Pb, –S–S– etc. bonds. Similar interactions have reported in the literature [61].

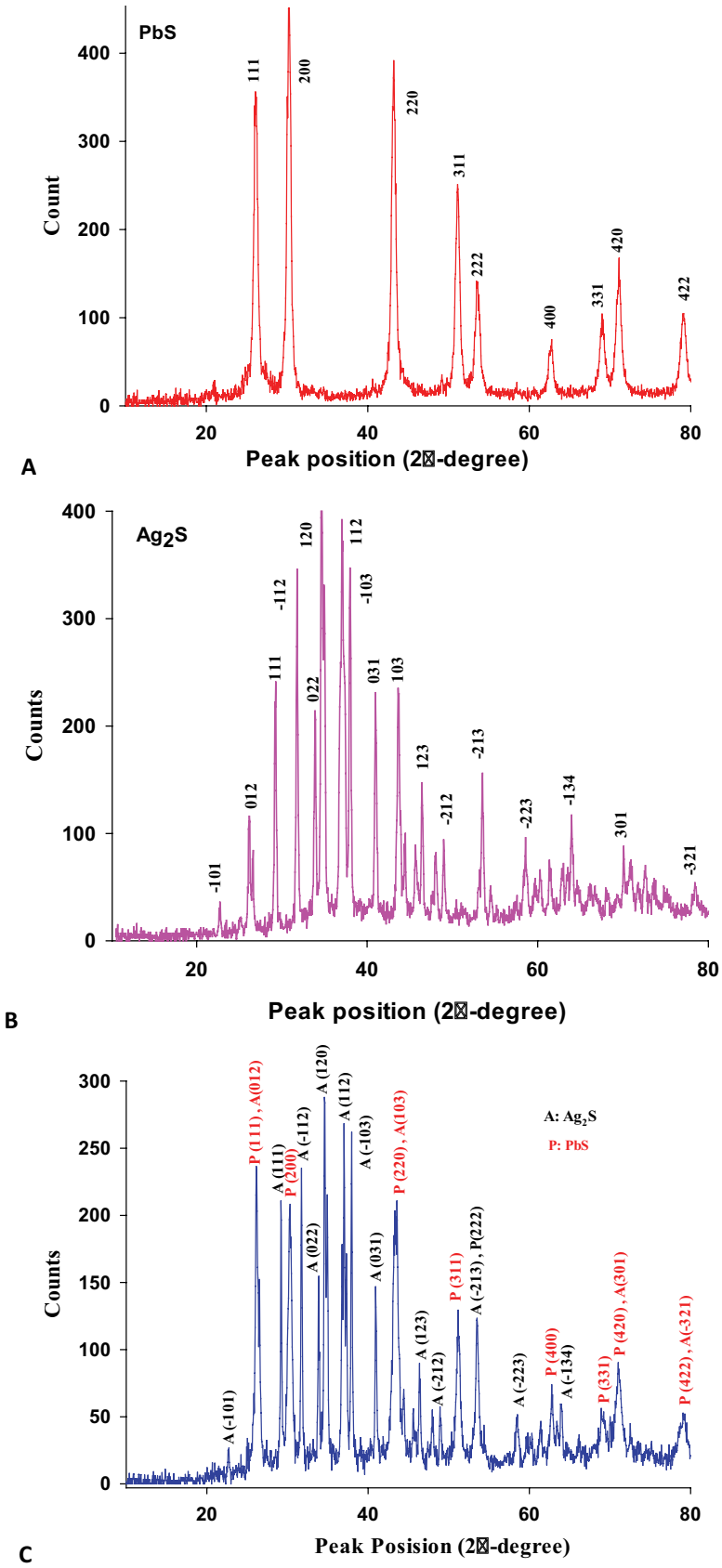

Fig. 1. Recorded XRD patterns of the (A) PbS NPs, (B) Ag_2S NPs, and (C) PbS–Ag_2S NC with a mole ratio of 1:2 PbS:Ag_2S.

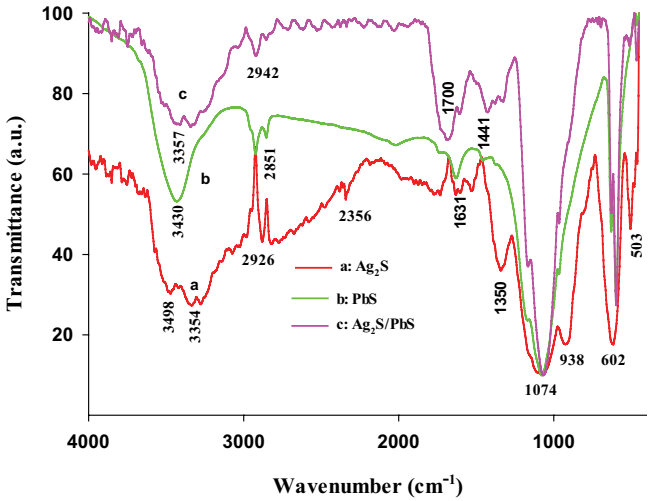

Fig. 2. FTIR spectra of the single PbS and Ag_2S NPs and the related PbS–Ag_2S NC.

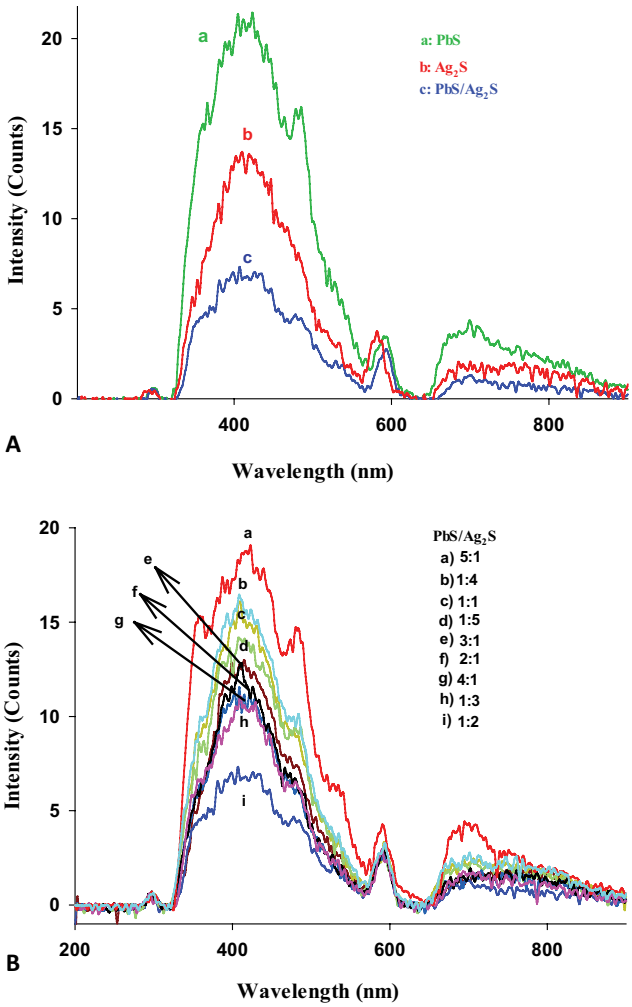

Fig. 3. (A) Photoluminescence (PL) spectra the single PbS and Ag_2S NPs and the related PbS–Ag_2S NC and (B) change in PL intensity of the PbS–Ag_2S NC as a function of mole ratio of the ingredients. Conditions in cases A and B – solvent: acetone; the amount of sample: 10 mg L^{-1}; excitation wavelength: 290 nm (ultrasonication conditions – frequency: 37 MHz; power: 100 W; mode: sweep during 20 min).

3.1.3. PL spectra

PL spectra of the single PbS and Ag_2S semiconductors and the related composite (suspension of 1 mg in 100 mL acetone) were recorded. When the samples were illuminated at an excitation wavelength of 290 nm, they emitted a broad peak in the range of 320–565 nm that centered at 410 nm. It was reported that when PbS cubic phase was irradiated at 368 nm, its PL peak was emitted at 418 nm [62]. PL peaks have reported for Ag_2S that centered at 520–530 nm [63]. In general, PL intensity is known as a measure of the rate of the e/h recombination. Thus, a higher PL intensity shows a faster e/h recombination process. As shown in Fig. 3A, the resulted coupled system showed a lower PL intensity than the single semiconductors. This confirms a lower e/h recombination for the coupled system that could result in a higher photodegradation activity for the coupled system.

Fig. 3B shows that the PL intensity of the resulted coupled systems depends on their Ag_2S/PbS mole ratios. This confirms that charge carrier separation in the coupled system varied with a change in the mentioned mole ratio. The lowest PL intensity was observed for the coupled system with the mole ratio of Ag_2S/PbS equal 2. It would be expected the highest photocatalytic activity for this catalyst which of results will discuss in the photodegradation section.

3.1.4. SEM results

Some SEM images of the single Ag_2S NPs (A,B), PbS NPs (C,D) and Ag_2S–PbS NC (E,F) are shown in Fig. 4. First of all, these images confirm nano-dimension for the as-synthesized systems. Images A and B show the formation of semi-spherical Ag_2S particles which relatively agglomerated in different directions. Images C and D show that PbS NPs have also disordered semi-spherical particles which their agglomeration created some sheet-like aggregates. In the SEM images of the composite (E and F) the mentioned nano-sheets are more obvious that belong to PbS species which covered by some semi-spherical Ag_2S species. A relative regular morphology was observed for the catalyst that shows the well-dispersion of Ag_2S and PbS ingredients thorough the catalyst.

3.1.5. UV-Vis diffuse reflectance spectroscopy

The bandgap energy (E_g) of a typical semiconductor relates to its electronic excitation which is a vital parameter in the semiconducting based photocatalytic degradation process. In general, a narrower E_g could result in the production of more photo-generated e/h pairs in the conduction band (C_B) and the valence band (V_B) of the illuminated semiconductor, respectively. Generally, the coupling of two or more semiconductors hybrids the energy levels and may cause a narrower E_g for the resulted composite or hetero-structure system [64]. In this work, to estimate the E_g values of the used single semiconductors and the resulted

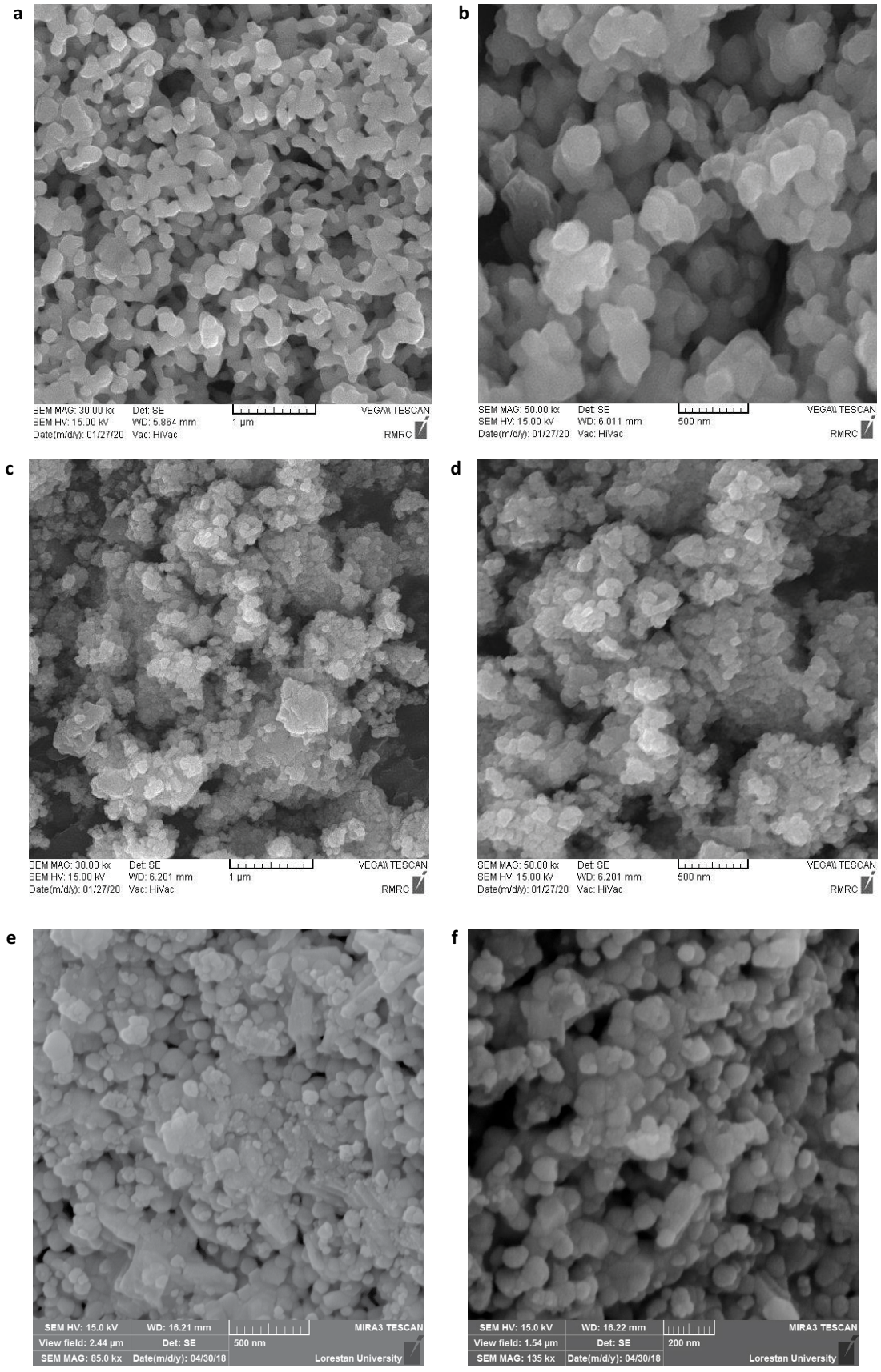

Fig. 4. SEM images of (A and B) Ag_2S NPs, (C and D) PbS NPs, and (E and F) the PbS–Ag_2S NC.

coupled system, the samples were subjected to UV-Vis DRS. Typical absorption spectra are shown in Fig. 5. In these spectra, the absorption edge wavelength (λ_{AE}) of each sample was estimated by extrapolation of the absorption curve (typically showed for curve b) back to *X*-axis. The estimated absorption edges, which correspond to the electronic excitation of samples, were substituted in the following equation and the bandgap energy (E_g) of the samples was estimated [65].

$$E_g\ (\text{eV}) = \frac{1{,}240}{\lambda_{AE}(\text{nm})} \tag{3}$$

To calculate the potential position of the V_B and C_B of the semiconductors, we used the electronegativity values of each sample. In the following equation, E_{VB} (V_B edge potential) was estimated by substituting of E_g, X (the geometric mean of the electronegativity of the constituent atoms in the investigated semiconductor) and E_e (the energy of free electrons relative to the normal hydrogen electrode (about 4.5 eV)) [66–69]:

$$E_{VB} = X - E_e + 0.5\,E_g \tag{4}$$

The electronegativity of a semiconductor is equal to the half value of the summation of the electron affinity (E_a) and the first ionization energy (E_i) of the element [70]. The E_{CB} value was estimated by using the $E_{CB} = E_{VB} - E_g$ formula [71]. All used [72–76] and the calculated values are summarized in Tables 1 and 2. As the results show, the coupling of the semiconductors, enhanced the optical properties of Ag_2S and caused a relative redshift in its bandgap. The obtained values for the potential positions of the C_B and V_B bands were used to draw the Schematic energy diagram to illustrate the charge carriers' transfer in the coupled system which of results will show in the next sections (photodegradation section).

3.1.6. Texture properties of the samples

The surface texture of the single and the composite samples were studied by the nitrogen adsorption–desorption isotherms as shown in Fig. 6A. The Brunauer–Emmett–Teller (BET) surface area of the as-synthesized compounds was investigated via these isotherms. The BET theory helps us to illustrate the physical adsorption of gaseous molecules on a solid surface and it is the base of an important analysis technique for measuring the specific surface area (SSA) of a solid material. SSA (or cross-sectional area) is an important property of a solid which defines as its total surface area per its unit mass cross-sectional area. For analyzing the pore structure, the N_2 adsorption–desorption isotherms must be recorded over the widest possible range of relative pressure, while allowing for slow equilibration and other operational problems, particularly at very low pressures. The smaller pores provide the larger surface area for gas adsorption. Barrett–Joyner–Halenda (BJH) analysis can also be used for measuring the pore area and specific pore volume based on the gas adsorption/desorption results. BJH characterizes pore size distribution independent of the external surface area due to the particle size of the sample.

The results obtained from the isotherms fitted to the BET equation and the BET plots constructed (Fig. 6B). S_{BET} was determined and summarized in Table 3 together with the pore area and specific pore volume obtained from BJH plots (Fig. 6C). The results are summarized in Table 3. As the results show, the characteristics of the composite sample located between those obtained for the single systems.

3.2. Degradation results

3.2.1. Boosted effect of the coupled system

Change in UV-Vis absorption spectra of PhP solution, as a measure of its removal extent, during different removal processes were recorded and the results are shown in Fig. 7A. The results showed that direct photolysis and surface adsorption have not a considerable role in PhP removal

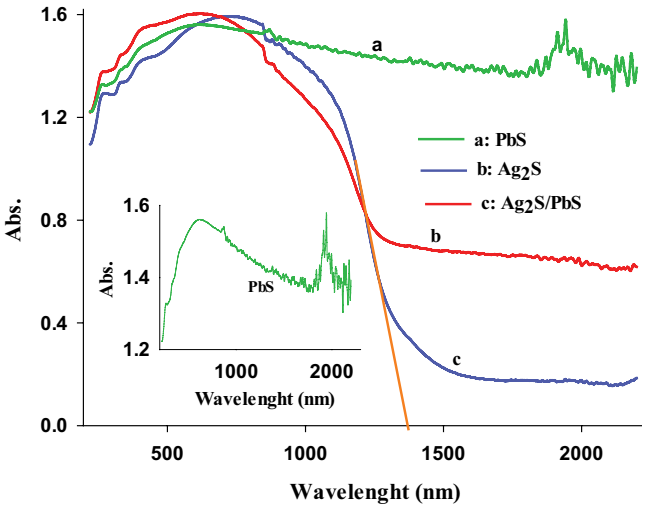

Fig. 5. Typical absorption spectra obtained in the UV-Vis DRS study of the samples.

Table 1
Mulliken electronegativity of the constituent elements of the used semiconductors by using their electron affinity (E_a) and the first ionization energy (E_i) in eV [47–51]

Element	E_a (eV)	E_i (eV)	½ (E_a + E_i) (eV)
Pb	0.356	7.416	3.886
S	2.071	10.36	6.218
Ag	1.305	7.576	4.440

Table 2
Bandgap energies and potential positions of V_B and C_B of the used semiconductors of the composite by using the empirical formula of $E_{VB} = X - E_0 + 0.5\,E_g$. X data are in Mulliken's electronegativity scale

Catalyst	X (eV)	E_g (eV)	E_g bulk (eV)	E_{VB} (eV)	E_{CB} (eV)
PbS	4.916	0.50	0.37	0.666	0.166
Ag_2S	4.967	0.89	0.92	0.912	0.022
PbS–Ag_2S	–	0.79	–	–	–

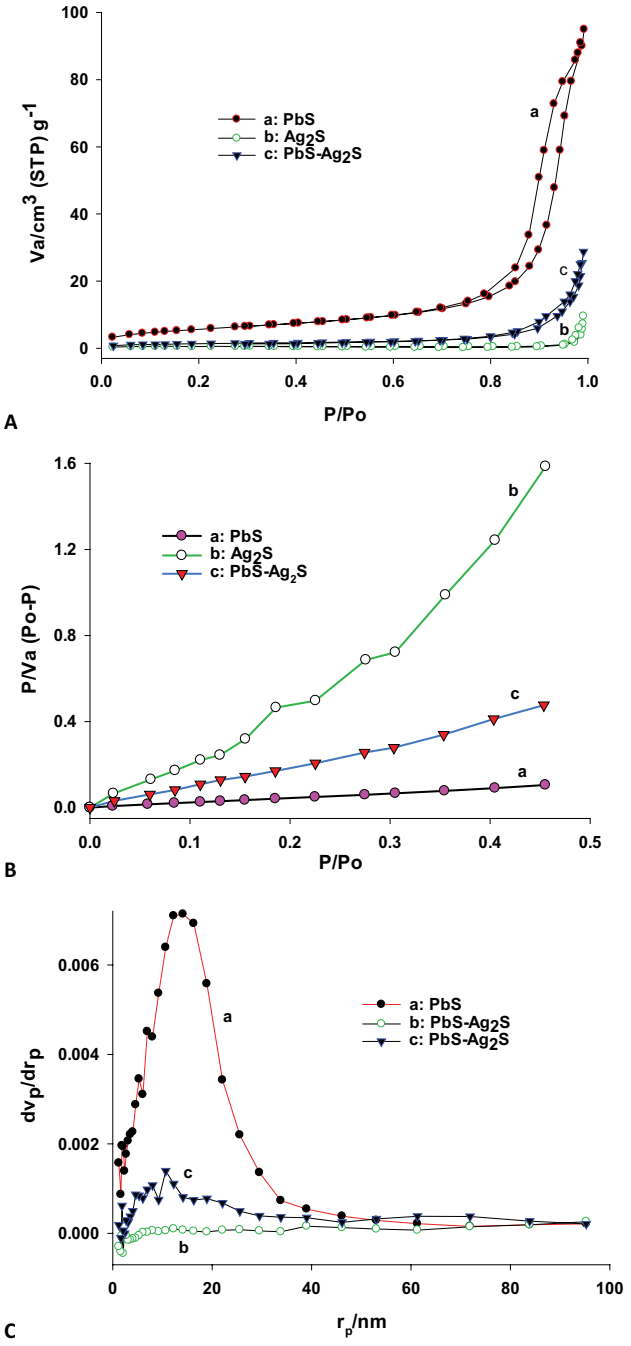

Fig. 6. (A) Typical N_2 adsorption–desorption isotherms, (B) BET, and (C) BJH plots for the single and composite systems.

Table 3
BET results obtained for the samples

Sample	A_{BET} ($m^2\ g^{-1}$)	Vp ($cm^3\ g^{-1}$)	dp (nm)
CdS	20.441	0.1434	27.9
Ag_2S	2.332	0.0109	20.4
CdS–Ag_2S	4.703	0.0425	36.3

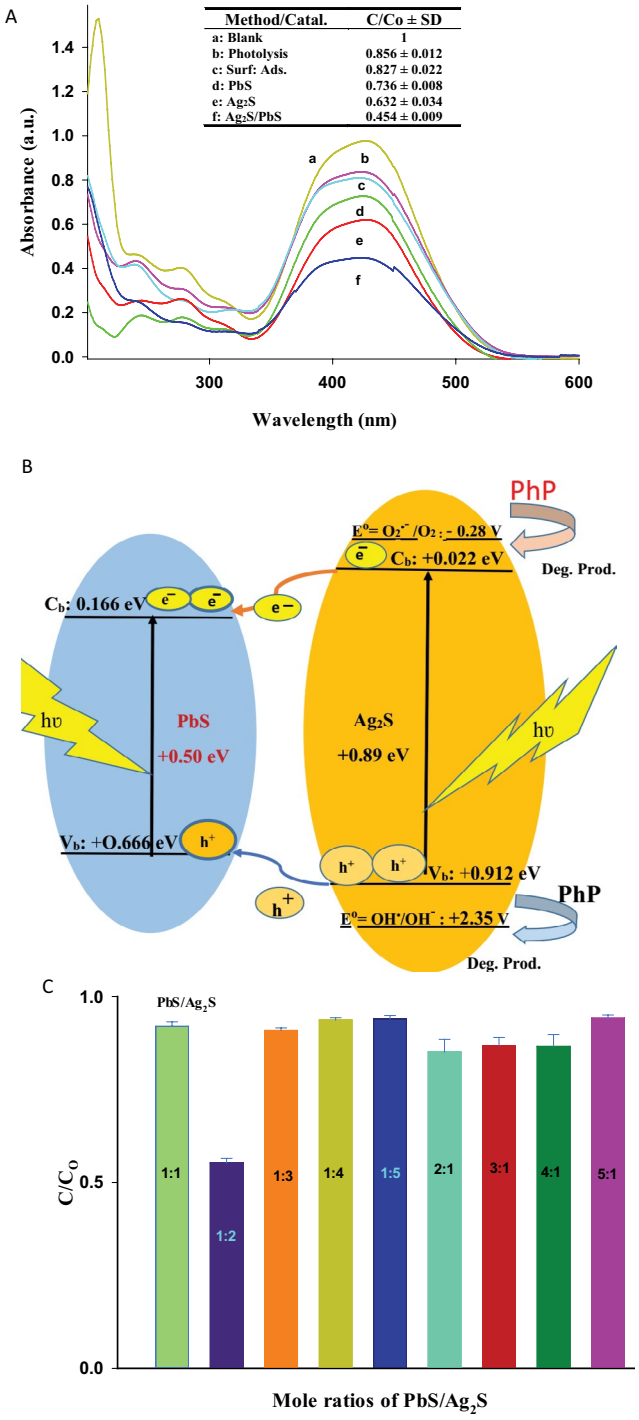

Fig. 7. (A) Results of removal of PZP by surface adsorption, direct photolysis and photocatalytic processes on the removal of PZP (catalysts dose: 0.5 g L^{-1}; C_{PZP}: 5 mg L^{-1}; time: 100 min; initial pH: 5.5), (B) Z-scheme for the charge carriers' transfer in the composite during the irradiation process, and (C) effects of the mole ratio of the PbS/Ag_2S in photodegradation of PhP at the aforementioned conditions.

during 100 min. At longer times (after 10 min), no enhancement on PhP removal was observed by the surface adsorption process. Hence, in the photocatalytic experiments, the

suspensions were shaken at dark for 10 min to achieve the equilibrium adsorption/desorption process and then the irradiation process was started.

Despite these methods, the photocatalysis process showed a significant enhancement in PhP removal at the same conditions. The trend of PbS–Ag_2S > Ag_2S > PbS was observed for the enhanced photocatalytic activity of the catalysts. The boosted the photocatalytic activity of the PbS–Ag_2S catalyst is related to the better charge separation process that occurred for it. This can be illustrated by the schematic diagram shown in Fig. 7B.

Under visible light illumination of the coupled system, both PbS and Ag_2S can be excited and produce e/h pairs. As shown, the produced photoelectrons in Ag_2S-C_B have more negative potential than that of PbS-C_B level. Thus, these electrons can be migrated into the PbS-C_B level. In contrast, the V_B levels of both semiconductors have suitable potential for hole transfer in the opposite trend. These charges carriers' transfer pathways drastically decreased the e/h recombination process and hence the photocatalytic activity was increased. As shown, the photogenerated electrons in C_B-levels of both semiconductors have suitable potentials to reduce dissolved oxygen into the superoxide radicals. The produced hole should oxidize water molecules or hydroxide ions into hydroxyl radicals. In consequence, by decreasing e/h recombination, the production of superoxide and hydroxyl radicals was increased [72–74].

3.2.2. Effect of Ag_2S/PbS mole ratio

Based on the above-mentioned discussion, it would be expected that change in the mole ratio of PbS/Ag_2S must affect the DE, because a matched mole ratio needs for a better e/h separation in the coupled system. Thus, photodegradation experiments were done by the coupled catalysts with different mole ratios. The results in Fig. 7C shows the best photocatalytic activity for the composite that its moles of Ag_2S were twice greater than that of PbS. This confirms that in this case, the best charge carriers' transfer can occur to separate e/h pairs. In this case, both production of e/h pairs in both semiconductors, especially in Ag_2S, and the separation of e/h pairs processes occur in optimal rates and thus the best photodegradation activity could be achieved [75].

3.2.3. Kinetic of the process

Commonly, the following Grotthuss–Draper law can use for the evaluation of the degradation rate of a typical pollutant in a case that the initial pollutant and its degradation intermediates absorb the arrived photons. This law is based on the Beer–Lambert law. In this equation, C_0 and C stand for the concentrations of pollutants at initial and final time t, k_1 is the rate constant, k_2 and k_3 are the absorption coefficients of the pollutant and the products, respectively [76,77].

$$-\frac{dC}{dt} = k_1\left(1-\exp\left[-\left(k_2C + k_3\left(C_0-C\right)\right)\right]\right)\left[\frac{k_2C}{\left(k_2C + k_3\left(C_0-C\right)\right)}\right] \quad (5)$$

A k_3 value of about zero means that the photodegradation products cannot absorb the arrived photons. A high concentration of the reactant, a zero-order kinetic would be expected for the process. The value of $k_3 \sim k_2$ means that the spectrum of degradation intermediates is similar to that of the reactant. In this case, a pseudo-first-order reaction rate (not a first-order one) would be considered for the kinetic of the process and hence Eq. (5) can be simplified to Eq. (6). In Eq. (6), k is the pseudo-first-order reaction rate constant [76–78].

$$-\frac{dC}{dt} = k_1\left(1-\exp\left[-k_2C_0\right]\right)\left(\frac{C}{C_0}\right) = kC \quad (6)$$

Getting the integral for Eq. (6) gives Eq. (7) that is similar to the pseudo-first-order reaction reported by Hinshelwood [79,80].

$$\ln\left(\frac{C}{C_0}\right) = -K_t\left(\text{or } C_t = C_0e^{-\text{kt}}\right) \quad (7)$$

In this work, photodegradation of PhP was followed at different irradiation times which of results are shown in Fig. 8. As shown in Fig. 8A, the absorbance of PhP solution was decreased at a maximum wavelength of 422 nm during the time. At initial times absorbance of the solution in the UV region was increased and decreased at longer times. This confirms the production of the smaller degradation intermediates that mineralized at longer times. Fig. 8B shows the plot of ln(C/C_0) vs. irradiation time to evaluate the kinetics of the process. Reasonable R^2-value confirms that the kinetics of the process obeys from the Hinshelwood pseudo-first-order rate reaction. The rate constant about 2.82×10^{-3} min^{-1} was obtained which resulted in a $t_{1/2}$ value of 246 min by using the $t_{1/2} = 0.693/k$ equation.

3.2.4. Chemical oxygen demand results

Commonly, the measure of pollution of an aquatic sample can be evaluated by the chemical oxygen demand (COD). This parameter shows the needed oxygen consumed for the oxidation of the organic pollutants present in media and a lower COD value shows lower polluted water [81].

To evaluate the mineralization extent of PZP solution during the photodegradation process, photodegradation experiments were done at the conditions mentioned in the caption of Fig. 9. The change in the COD value of the solution is shown in Fig. 9A. The degradation extent of PZP was calculated by recording the absorption spectra of the resulted solutions. Based on the results, the plot of ln(C/C_0) vs. time (Fig. 9B) was drawn ($y = -1.83 \times 10^{-3}$–1.80×10^{-3} x), which shows a rate constant value about 1.80×10^{-3} min^{-1} for the degradation of PZP. This value corresponds to $t_{1/2}$ = 385 min for the photodegradation of PZP during 50 min irradiation time.

Based on the COD results of the solutions, the kinetic of the process was followed (Fig. 9C). The resulted plot had a line equation of $y = -1.65 \times 10^{-3}$–1.41×10^{-3} x. The k-value of 1.41×10^{-3} for the mineralization of the PZP solution shows

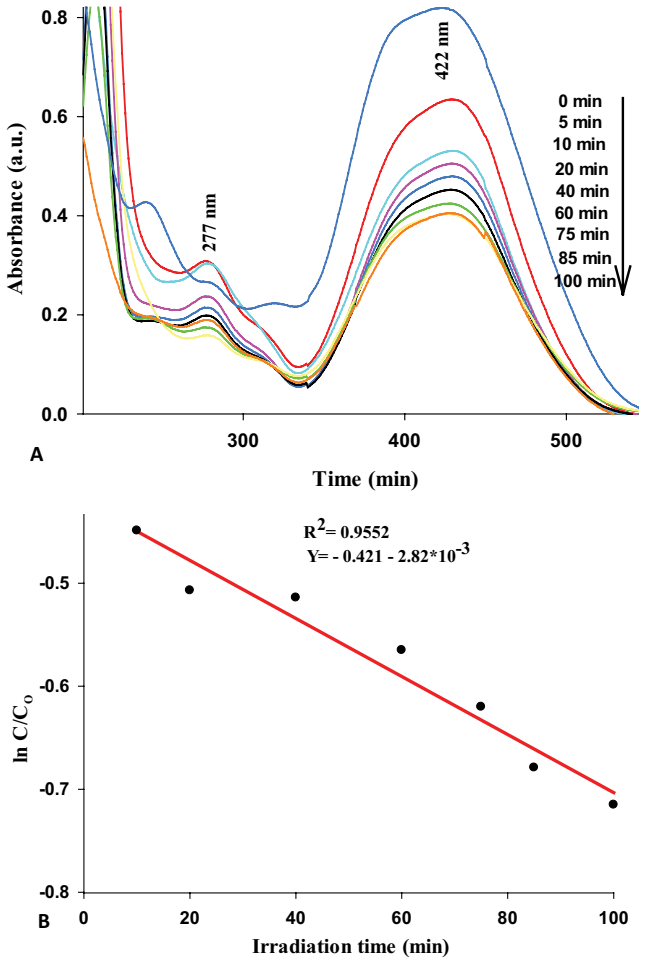

Fig. 8. (A) Change in absorption spectra of PZP during different photodegradation times by the PbS–Ag_2S catalyst (dose of the catalyst: 0.5 g L^{-1}; C_{PZP} = 5 mg L^{-1}; pH 7) and (B) resulted ln(C/C_0) – time plot for the evaluation of the kinetic of the process.

a $t_{1/2}$ value of 495 min for its mineralization during the process. The results show the degradation of PhP molecules is 1.28 times greater than its mineralization extent for 50 min. This shows that there are some degradation intermediates that resist further mineralization during this time and need a longer time for mineralization.

4. Conclusion

Coupling of PbS and Ag_2S semiconductors resulted to an enhanced photocatalytic activity towards PZP in aqueous solution. The coupled system showed the lowest PL intensity with respect to the single systems, confirming a lower e/h recombination. This caused the aforementioned boosted photocatalytic activity for this system. Both photocatalytic activity and PL intensity depended on the mole ratio of Ag_2S:CdS and thus the best results were obtained for the coupled system that its moles of Ag_2S were twice greater than that of PbS. The mineralization extent of the PZP molecules was followed by the COD technique. Based on the COD results a rate constant of 1.41 × 10^{-3} was obtained for

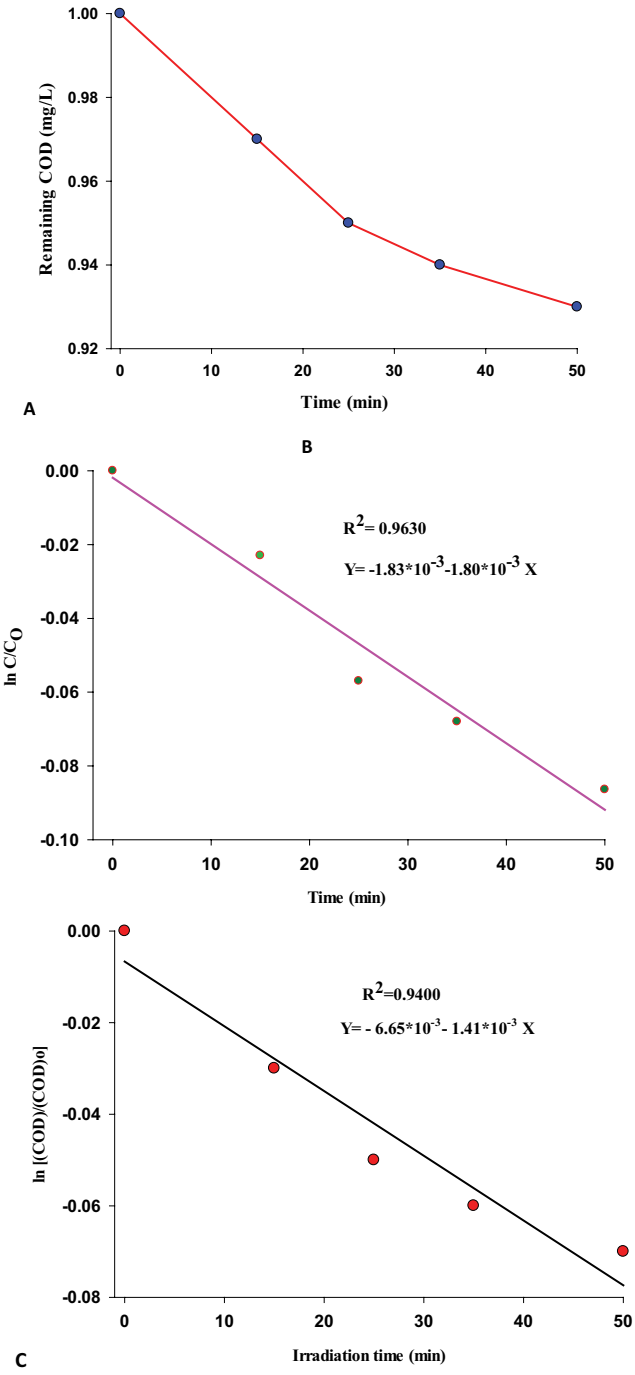

Fig. 9. (A) Change in COD values of PZP solution during its photodegradation. Typical plots for the study of kinetics of the process based on (B) absorbencies of solution based on UV-Vis spectra and (C) mineralization rate of PZP obtained based on COD results. Conditions in photodegradation experiments: dose of the catalyst: 0.7 g L^{-1}; C_{PZP} = 5 mg L^{-1}, pH 7).

the mineralization of PZP solution during 50 min irradiation time, while the value of 1.80 × 10^{-3} min^{-1} was obtained for its degradation extent at the same time. This shows that the degradation of PZP molecules is 1.3 times greater than its mineralization extent during this time. On the other hand, some

degradation intermediates may resist further mineralization at this time and need a longer time for more mineralization extent.

References

[1] X.X. Su, D.F. Wu, Facile construction of the phase junction of BiOBr and $Bi_4O_5Br_2$ nanoplates for ciprofloxacin photodegradation, Mater. Sci. Semicond. Process., 80 (2018) 123–130.

[2] A. Heidarineko, A. Bagheri Ghomi, *P*-type semiconducting NiO nanoparticles synthesis and its photocatalytic activity, Iran. J. Catal., 7 (2017) 277–282.

[3] J. Singh, M. Sharma, S. Basu, Heavy metal ions adsorption and photodegradation of remazol black XP by iron oxide/silica monoliths: kinetic and equilibrium modelling, Adv. Powder Technol., 29 (2018) 2268–2279.

[4] D.-L. Guan, C.-G. Niu, X.-J. Wen, H. Guo, C.-H. Deng, G.-M. Zeng, Enhanced *Escherichia coli* inactivation and oxytetracycline hydrochloride degradation by a Z-scheme silver iodide decorated bismuth vanadate nanocomposite under visible light irradiation, J. Colloid Interface Sci., 512 (2018) 272–281.

[5] M. Taei, F. Hasanpour, M. Dinari, E. Dehghani, Au nanoparticles decorated reduced graphene oxide/layered double hydroxide modified glassy carbon as a sensitive sensor for electrocatalytic determination of phenazopyridine, Measurement, 99 (2017) 90–97.

[6] R. Pandimurugan, S. Thambidurai, Novel seaweed capped ZnO nanoparticles for effective dye photodegradation and antibacterial activity, Adv. Powder Technol., 27 (2016) 1062–1072.

[7] H.R. Pouretedal, A.M. Sohrabi, Photosensitization of TiO_2 by ZnS and bromo thymol blue and its application in photodegradation of para-nitrophenol, J. Iran. Chem. Soc., 13 (2016) 73–79.

[8] E.M.S. Azzam, N.A. Fathy, S.M. El-Khouly, R.M. Sami, Enhancement the photocatalytic degradation of methylene blue dye using fabricated CNTs/TiO_2/AgNPs/Surfactant nanocomposites, J. Water Process Eng., 28 (2019) 311–321.

[9] N. Ajoudanian, A. Nezamzadeh-Ejhieh, Enhanced photocatalytic activity of nickel oxide supported on clinoptilolite nanoparticles for the photodegradation of aqueous cephalexin, Mater. Sci. Semicond. Process., 36 (2015) 162–169

[10] V.K. Gupta, A. Fakhri, M. Azad, S. Agarwal, Synthesis and characterization of Ag doped ZnS quantum dots for enhanced photocatalysis of Strychnine as a poison: charge transfer behavior study by electrochemical impedance and time-resolved photoluminescence spectroscopy, J. Colloid Interface Sci., 510 (2018) 95–102.

[11] K. Thirumalai, S. Balachandran, M. Swaminathan, Superior photocatalytic, electrocatalytic, and self-cleaning applications of fly ash supported ZnO nanorods, Mater. Chem. Phys., 183 (2016) 191–200.

[12] M.A. Dadvar, R. Fazaeli, Application of sodium titanate nanotubes doped with vanadium (VNaTNT) as a heterogeneous catalyst for oxidation of sulfides at room temperature, Chin. J. Catal., 37 (2016) 494–501.

[13] S. Ahmad Bhat, F. Zafar, A. Hossain Mondal, A. Kareem, A. Ullah Mirza, S. Khan, A. Mohammad, Q. Mohd. Rizwanul Haq, N. Nishat, Photocatalytic degradation of carcinogenic Congo red dye in aqueous solution, antioxidant activity and bactericidal effect of NiO nanoparticles, J. Iran. Chem. Soc., 17 (2020) 215–227.

[14] H. Aliyan, R. Fazaeli, R. Jalilian, Fe_3O_4@mesoporous SBA-15: a magnetically recoverable catalyst for photodegradation of malachite green, Appl. Surf. Sci., 276 (2013) 147–153.

[15] A. Khataee, D. Kalderis, P. Gholami, A. Fazli, M. Moschogiannaki, V. Binas, M. Lykaki, M. Konsolakis, Cu_2O-CuO@ biochar composite: synthesis, characterization and its efficient photocatalytic performance, Appl. Surf. Sci., 498 (2019) 143846.

[16] I.R. Segundo, E. Freitas, S. Landi Jr., M.F.M. Costa, J.O. Carneiro, Smart, Photocatalytic and self-cleaning asphalt mixtures: a literature review, Coatings, 9 (2019) 696 (1–22 pages).

[17] B.N. Rashmi, S.F. Harlapur, B. Avinash, C.R. Ravikumar, H.P. Nagaswarupa, M.R. Anil Kumar, K. Gurushantha, M.S. Santosh, Facile green synthesis of silver oxide nanoparticles and their electrochemical, photocatalytic and biological studies, Inorg. Chem. Commun., 111 (2020) 107580.

[18] L. Shabani, H. Aliyan, Synthesis and photocatalytic activity of nanosized modified mesocellulous silica foams (MCFs) with PW12 and vanadium oxide, Iran. J. Catal., 6 (2016) 221–228.

[19] K. Prakash, S. Karuthapandian, S. Senthilkumar, Zeolite nanorods decorated g-C_3N_4 nanosheets: a novel platform for the photodegradation of hazardous water contaminants, Mater. Chem. Phys., 221 (2019) 34–46.

[20] P. Raizada, J. Kumari, P. Shandilya, P. Singh, Kinetics of photocatalytic mineralization of oxytetracycline and ampicillin using activated carbon supported ZnO/$ZnWO_4$ nanocomposite in simulated wastewater, Desal. Water Treat., 79 (2017) 204–213.

[21] S. Dianat, Visible light induced photocatalytic degradation of direct red 23 and direct brown 166 by $InVO_4$-TiO_2 nanocomposite, Iran. J. Catal., 8 (2018) 121–132.

[22] M. Padervand, E. Jalilian, R. Majdani, M. Goshadezehn, BiOCl/AgCl-BiOI/AgI quaternary nanocomposite for the efficient photodegradation of organic wastewaters and pathogenic bacteria under visible light, J. Water Process Eng., 29 (2019) 100789.

[23] H.R. Pouretedal, M. Kiyani, Photodegradation of 2-nitrophenol catalyzed by CoO, CoS and CoO/CoS nanoparticles, J. Iran. Chem. Soc., 11 (2014) 271–277.

[24] S. Ghattavi, A. Nezamzadeh-Ejhieh, A brief study on the boosted photocatalytic activity of AgI/WO_3/ZnO in the degradation of Methylene Blue under visible light irradiation, Desal. Water Treat., 166 (2019) 92–104.

[25] M. Karimi-Shamsabadi, M. Behpour, A. Kazemi Babaheidari, Z. Saberi, Efficiently enhancing photocatalytic activity of NiO-ZnO doped onto nanozeoliteX by synergistic effects of *p-n* heterojunction, supporting and zeolite nanoparticles in photo-degradation of Eriochrome Black T and Methyl Orange, J. Photochem. Photobiol., A, 346 (2017) 133–143.

[26] S. Landi Jr., J. Carneiro, S. Ferdov, A.M. Fonseca, I.C. Neves, M. Ferreira, P. Parpot, O.S.G.P. Soares, M.F.R. Pereira, Photocatalytic degradation of Rhodamine B dye by cotton textile coated with SiO_2-TiO_2 and SiO_2-TiO_2-HY composites, J. Photochem. Photobiol., A, 346 (2017) 60–69.

[27] M.L. Maya-Treviño, J.L. Guzmán-Mar, L. Hinojosa-Reyes, A. Hernández-Ramírez, Synthesis and photocatalytic activity of ZnO-CuPc for methylene blue and potassium cyanide degradation, Mater. Sci. Semicond. Process., 77 (2018) 74–82.

[28] G.C. Chen, M.M. Zhu, X.W. Wei, Photocatalytic properties of attached BiOCl-(001) nanosheets onto AgBr colloidal spheres toward MO and RhB degradation under an LED irradiation, Mater. Lett., 212 (2018) 182–185.

[29] S. Majumder, A.C. Mendhe, B.R. Sankapal, Nanoheterojunction through PbS nanoparticles anchored CdS nanowires towards solar cell application, Int. J. Hydrogen Energy, 44 (2019) 7095–7107.

[30] X.S. Zhao, I. Gorelikov, S. Musikhin, S. Cauchi, V. Sukhovatkin, E.H. Sargent, E. Kumacheva, Synthesis and optical properties of thiol-stabilized PbS nanocrystals, Langmuir, 21 (2005) 1086–1090.

[31] L.F. Koao, F.B. Dejene, H.C. Swart, Synthesis of PbS nanostructures by chemical bath deposition method, Int. J. Electrochem. Sci., 9 (2014) 1747–1757.

[32] D. Ayodhya, G. Veerabhadram, Sunlight-driven competent photocatalytic degradation of crystal violet using sonochemically produced GO capped Ag_2S nanocomposites, Mater. Today Commun., 19 (2019) 157–169.

[33] C.L. Yu, L.F. Wei, W.Q. Zhou, D.D. Dionysiou, L.H. Zhu, Q. Shu, H. Liu, A visible-light-driven core-shell like Ag_2S@ Ag_2CO_3 composite photocatalyst with high performance in pollutants degradation, Chemosphere, 157 (2016) 250–261.

[34] J. Liu, L.Q. Jing, G.F. Gao, Y.Q. Xu, M. Xie, L.Y. Huang, H.Y. Ji, J.M. Xie, H.M. Li, Ag_2S quantum dots *in situ* coupled to hexagonal SnS2 with enhanced photocatalytic activity for MO and Cr(VI) removal, RSC Adv., 7 (2017) 46823–46831.

[35] X. Li, D. Shen, C. Liu, J.Z. Li, Y. Zhou, X.H. Song, P.W. Huo, H.Q. Wang, Y.S. Yan, Fabricated rGO-modified Ag_2S nanoparticles/g-C_3N_4 nanosheets photocatalyst for enhancing photocatalytic activity, J. Colloid Interface Sci., 554 (2019) 468–478.
[36] Y. Zeng, N. Guo, H.Y. Li, Q.Y. Wang, X.J. Xu, Y. Yu, X.R. Han, H.W. Yu, Construction of flower-like MoS_2/Ag_2S/Ag Z-scheme photocatalysts with enhanced visible-light photocatalytic activity for water purification, Sci. Total Environ., 659 (2019) 20–32.
[37] A. Shafi, N. Ahmad, S. Sultana, S. Sabir, M.Z. Khan, Ag_2S-Sensitized NiO-ZnO heterostructures with enhanced visible light photocatalytic activity and acetone sensing property, ACS Omega, 4 (2019) 12905–12918.
[38] H. Mossalayi, A. Moghimi, Fabrication of TiO_2/Ag_2S nanocomposites via a new method for photocatalytic degradation of *p*-xylene & chlorophenol, J. Chem. Pharm. Res., 3 (2011) 718–724.
[39] J.W. Huang, C.L. Yang, Q. Song, D.X. Liu, L. Li, Photocatalytic performance of Ag_2S/ZnO/ZnS nanocomposites with high visible light response prepared via microwave-assisted hydrothermal two-step method, Water Sci. Technol., 78 (2018) 1802–1811.
[40] W.L. Ong, G.W. Ho, Enhanced photocatalytic performance of TiO_2 hierarchical spheres decorated with Ag_2S nanoparticles, Procedia Eng., 141 (2016) 7–14.
[41] K. Hedayati, M. Kord, M. Goodarzi, D. Ghanbari, S. Gharigh, Photo-catalyst and magnetic nanocomposites: hydrothermal preparation of core–shell Fe_3O_4@PbS for photo-degradation of toxic dyes, J. Mater. Sci. - Mater. Electron., 28 (2017) 1577–1589.
[42] R.M. Mohamed, E.S. Aazam, New visible-light Pt/PbS nanoparticle photocatalysts for the photocatalytic oxidation of thiophene, Clean – Soil Air Water, 42 (2014) 1–6.
[43] P.A. Ajibade, A.E. Oluwalana, Synthesis and crystal structure of bis(O-methyl hydrogenato carbonodithioate)-Pb(II): structural, optical and photocatalytic studies of PbS nanoparticles from the complex, J. Coord. Chem., 27 (2019) 3575–3588.
[44] M. Babaahamdi-Milani, A. Nezamzadeh-Ejhieh, A comprehensive study on photocatalytic activity of supported Ni/Pb sulfide and oxide systems onto natural zeolite nanoparticles, J. Hazard. Mater., 318 (2016) 291–301.
[45] H.-J. Wang, Y. Cao, L.-L. Wu, S.-S. Wu, A. Raza, N. Liu, J.-Y. Wang, T. Miyazawa, ZnS-based dual nano-semiconductors (ZnS/PbS, ZnS/CdS or ZnS/Ag_2S): a green synthesis route and photocatalytic comparison for removing organic dyes, J. Environ. Chem. Eng., 6 (2018) 6771–6779.
[46] Q.Y. Wang, R.C. Jin, C.L. Yin, M.J. Wang, J.F. Wang, S.M. Gao, Photoelectrocatalytic removal of dye and Cr(VI) pollutants with Ag_2S and Bi_2S_3 co-sensitized TiO_2 nanotube arrays under solar irradiation, Sep. Purif. Technol., 172 (2017) 303–309.
[47] W. Liu, J. Zhang, Z.H. Peng, X.H. Yang, L. Li, Q.S. Chen, J.B. Liu, K.M. Wang, Controlled formation of Ag_2S/Ag Janus nanoparticles using alkylamine as reductant surfactants, Colloids Surf., A, 544 (2018) 111–117.
[48] D.W. Fan, H.Y. Wang, M.S. Khan, C.Z. Bao, H. Wang, D. Wu, Q. Wei, B. Du, An ultrasensitive photoelectrochemical immunosensor for insulin detection based on BiOBr/Ag_2S composite by in-situ growth method with high visible-light activity, Biosens. Bioelectron., 97 (2017) 253–259.
[49] H.-J. Wang, X.-H. Yu, Y. Cao, B. Zhou, C.-F. Wang, Controllable synthesis and adjustable antineoplastic activity of bovine serum albumin-conjugated PbS/Ag_2S core/shell nano-composites, J. Inorg. Biochem., 113 (2012) 40–46.
[50] K. Hedayati, M. Goodarzi, M. Kord, Green and facile synthesis of Fe_3O_4-PbS magnetic nanocomposites applicable for the degradation of toxic organic dyes, Main Group Met. Chem., 39 (2016) 183–194.
[51] V. Ramasamy Raja, D. Rani Rosaline, A. Suganthi, M. Rajarajan, Facile fabrication of PbS/MoS_2 nanocomposite photocatalyst with efficient photocatalytic activity under visible light, Solid State Sci., 13 (2017) 1293–2558.
[52] Z.-D. Meng, L. Zhu, K. Ullah, S. Ye, Q. Sun, W.-C. Oh, Enhanced visible light photocatalytic activity of Ag_2S-graphene/TiO_2 nanocomposites made by sonochemical synthesis, Chin. J. Catal., 34 (2013) 1527–1533.
[53] H.R. Pouretedal, M. Fallahgar, F.S. Pourhasan, M. Nasiri, Taguchi optimization of photodegradation of yellow water of trinitrotoluene production catalyzed by nanoparticles TiO_2/N under visible light, Iran. J. Catal., 7 (2017) 317–326.
[54] W.X. Zhang, L. Zhang, Z.H. Hui, X.M. Zhang, Y.T. Qian, Synthesis of nanocrystalline Ag_2S in aqueous solution, Solid State Ionics, 130 (2000) 111–114.
[55] K. Kalpana, V. Selvaraj, ZnS/SnS/Ag_2S photocatalyst with enhanced photocatalytic activity under visible light illumination towards wastewater treatment, Res. Chem. Intermed., 43 (2017) 423–435.
[56] R. Gaur, P. Jeevanandam, PbS micro-nanostructures with controlled morphologies by a novel thermal decomposition approach, J. Nanopart. Res., 18 (2016), https://doi.org/10.1007/s11051–016–3382–5.
[57] S. Dharmraj Khairnar, M. Rajendra Patil, V. Shankar Shrivastava, Hydrothermally synthesized nanocrystalline Nb_2O_5 and its visible-light photocatalytic activity for the degradation of congo red and methylene blue, Iran. J. Catal., 8 (2018) 143–150.
[58] P. Scherrer, Bestimmung der Grösse und der inneren Struktur von Kolloidteilchen mittels Röntgensrahlen [Determination of the size and internal structure of colloidal particles using X-rays], Nachr Ges Wiss Goettingen, Math-Phys Kl. 1918, 1918, pp. 98-100 (in German).]
[59] A.V. Borhade, B.K. Uphade, A comparative study on characterization and photocatalytic activities of PbS and co doped PbS nanoparticles, Chalcogenide Lett., 9 (2012) 299–306.
[60] VH.-J. Wang, X.-H. Yu, Y. Cao, B. Zhou, C.-F. Wang, Controllable synthesis and adjustable antineoplastic activity of bovine serum albumin-conjugated PbS/Ag_2S core/shell nano-composites, J. Inorg. Biochem., 113 (2012) 40–46.
[61] R. Zamiri, H. Abbastabar Ahangar, A. Zakaria, G. Zamiri, M. Shabani, B. Singh, J.M.F. Ferreira, The structural and optical constants of Ag_2S semiconductor nanostructure in the Far-Infrared, Chem. Cent. J., 9 (2015) 28–34.
[62] H.-J. Wang, Y. Cao, L.-L. Wu, S.-S. Wu, A. Raza, N. Liu, J.-Y. Wanga, T. Miyazawa, ZnS-based dual nano-semiconductors (ZnS/PbS, ZnS/CdS or ZnS/Ag_2S,): a green synthesis route and photocatalytic comparison for removing organic dyes, J. Environ. Chem. Eng., 6 (2018) 6771–6779.
[63] M. Abbasi, U. Rafique, G. Murtaza, M. Aqeel Ashraf, Synthesis, characterisation and photocatalytic performance of ZnS coupled Ag_2S nanoparticles: a remediation model for environmental pollutants, Arabian J. Chem., 11 (2018) 827–837.
[64] D.F. Zhang, G.Z. Zhang, Q. Wang, L. Zhang, Dual-functional catalytic materials: magnetically hollow porous Ni-manganese oxides microspheres/cotton cellulose fiber, J. Taiwan Inst. Chem. Eng., 77 (2017) 311–320.
[65] M. Pirhashemi, A. Habibi-Yangjeh, ZnO/$NiWO_4$/Ag_2CrO_4 nanocomposites with *p-n-n* heterojunctions: highly improved activity for degradations of water contaminants under visible light, Sep. Purif. Technol., 193 (2018) 69–80.
[66] N. Omrani, A. Nezamzadeh-Ejhieh, Focus on scavengers' effects and GC-MASS analysis of photodegradation intermediates of sulfasalazine by Cu_2O/CdS nanocomposite, Sep. Purif. Technol., 235 (2020) 116228.
[67] M. Pirhashemi, A. Habibi-Yangjeh, Ultrasonic-assisted preparation of plasmonic ZnO/Ag/Ag_2WO_4 nanocomposites with high visible-light photocatalytic performance for degradation of organic pollutants, J. Colloid Interface Sci., 491 (2017) 216–229.
[68] H.N. Che, G.B. Che, E.H. Jiang, C.B. Liu, H.J. Dong, C.M. Li, A novel Z-Scheme CdS/Bi_3O_4Cl heterostructure for photocatalytic degradation of antibiotics: mineralization activity, degradation pathways and mechanism insight, J. Taiwan Inst. Chem. Eng., 91 (2018) 224–234.
[69] Z.F. Ye, J.Z. Li, M.J. Zhou, H.Q. Wang, Y. Ma, P.W. Huo, L.B. Yu, Y.S. Yan, Well-dispersed nebula-like ZnO/CeO_2@HNTs heterostructure for efficient photocatalytic degradation of tetracycline, Chem. Eng. J., 304 (2016) 917–933.
[70] D.R. Lide, Ed., CRC Handbook of Chemistry and Physics, Section 10, Atomic, Molecular, and Optical Physics Ionization

Potentials of Atoms and Atomic Ions, 84th ed., CRC Press, Boca Raton, Florida, 2003.
[71] T.Y. Wang, W. Quan, D. Jiang, L.L. Chen, D. Li, S. Meng, M. Chen, Synthesis of redox-mediator-free direct Z-scheme AgI/WO_3 nanocomposite photocatalysts for the degradation of tetracycline with enhanced photocatalytic activity, Chem. Eng. J., 300 (2016) 280–290.
[72] M. Karimi-Shamsabadi, A. Nezamzadeh-Ejhieh, Comparative study on the increased photoactivity of coupled and supported manganese-silver oxides onto a natural zeolite nano-particles, J. Mol. Catal. A: Chem., 418 (2016) 103–114.
[73] Z.Y. Lu, Z.H. Yu, J.B. Dong, M.S. Song, Y. Liu, X.L. Liu, Z.F. Ma, H. Su, Y.S. Yan, P.W. Huo, Facile microwave synthesis of a Z-scheme imprinted $ZnFe_2O_4$/Ag/PEDOT with the specific recognition ability towards improving photocatalytic activity and selectivity for tetracycline, Chem. Eng. J., 337 (2018) 228–241.
[74] P. Dhiman, Mu. Naushad, K.M. Batoo, A. Kumar, G. Sharma, A.A. Ghfar, G. Kumar, M. Singh, Nano $Fe_xZn_{1-x}O$ as a tuneable and efficient photocatalyst for solar powered degradation of bisphenol A from aqueous environment, J. Cleaner Prod., 165 (2017) 1542–1556.
[75] P. Mohammadyari, A. Nezamzadeh-Ejhieh, Supporting of mixed ZnS–NiS semiconductors onto clinoptilolite nano-particles to improve its activity in photodegradation of 2-nitrotoluene, RSC Adv., 5 (2015) 75300–75310.
[76] I. Matsuura, M. Imaizumi, M. Sugiyama, Method of kinetic analysis of photodegradation: Nifedipine in solutions, Chem. Pharm. Bull., 38 (1990) 1692–1696.
[77] C.Y. Lu, X. Yin, X.F. Liu, M.H. Wang, Study of the photodegradation kinetics and pathways of Hexaflumuron in liquid media, Photochem. Photobiol., 90 (2014) 1219–1223.
[78] N. Omrani, A. Nezamzadeh-Ejhieh, M. Alizadeh, Brief study on the kinetic aspect of photodegradation of sulfasalazine aqueous solution by cuprous oxide/cadmium sulfide nano-particles, Desal. Water Treat., 162 (2019) 290–302.
[79] S. Mousavi-Mortazavi, A. Nezamzadeh-Ejhieh, Supported iron oxide onto an Iranian clinoptilolite as a heterogeneous catalyst for photodegradation of furfural in a wastewater sample, Desal. Water Treat., 57 (2016) 10802–10814.
[80] B. Divband, A. Jodaei, M. Khatamian, Enhancement of photocatalytic degradation of 4-nitrophenol by integrating Ag nanoparticles with ZnO/HZSM-5 nanocomposite, Iran. J. Catal., 9 (2019) 63–70.
[81] J. Saien, A.R. Soleymani, Comparative investigations on nano and micro titania photocatalysts in degradation and mineralization: use of turbidity in kinetic studies, J. Iran. Chem. Soc., 6 (2009) 602–611.

Supplementary information

SDT1: results used in Scherrer equations for the estimation of the crystallite size single Ag_2S and PbS NPs and the Ag_2S–PbS NC

2θ	FWHM (2θ)	β	cosθ	β cosθ	*d* (nm)	Av. *d* (nm)
For Ag_2S NPs						
26.6	0.148	0.0026	0.999	0.0026	55.44	34.3 ± 10.5
29	0.246	0.0043	0.999	0.0043	32.23	
32	0.197	0.0034	0.999	0.0034	40.76	
34.8	0.148	0.0026	0.999	0.0026	53.31	
38	0.246	0.0043	0.999	0.0043	32.23	
44	0.197	0.0034	0.999	0.0034	40.76	
45.7	0.295	0.0052	0.999	0.0052	26.65	
46.5	0.246	0.0043	0.999	0.0043	32.23	
48	0.246	0.0043	0.999	0.0043	32.23	
49	0.197	0.0034	0.999	0.0034	40.76	
53.5	0.246	0.0043	0.999	0.0043	32.23	
58.5	0.492	0.0086	0.999	0.0086	16.12	
61	0.394	0.0069	0.999	0.0069	20.09	
64	0.246	0.0043	0.999	0.0043	32.23	
72.5	0.295	0.0052	0.999	0.0052	26.65	
For PbS NPs						
26.08	0.197	0.003	0.999	0.003	40.29	23.1 ± 10.3
30.24	0.148	0.026	0.999	0.003	53.30	
43.20	0.393	0.007	0.999	0.007	20.09	
51.15	0.541	0.009	0.999	0.009	14.74	
53.61	0.590	0.010	0.999	0.010	13.86	
62.70	0.590	0.010	0.999	0.010	13.86	
69.04	0.492	0.009	0.999	0.009	16.12	
71.10	0.689	0.001	0.999	0.001	11.55	
79.10	0.344	0.006	0.999	0.006	23. 1	
For Ag_2S–PbS NC						
26	0.246	0.0043	0.999	0.0043	32.31	33.5 ± 10.5
29	0.148	0.0026	0.999	0.0026	53.93	
30	0.394	0.0069	0.999	0.0069	20.17	
31.7	0.197	0.0034	0.999	0.0034	40.41	
34	0.197	0.0034	0.999	0.0034	40.41	
34.7	0.148	0.0043	0.999	0.0043	32.31	
37	0.098	0.0017	0.999	0.0017	80.58	
38	0.197	0.0034	0.999	0.0034	40.41	
41	0.197	0.0034	0.999	0.0034	40.41	
43.4	0.590	0.0103	0.999	0.0103	13.46	
46.4	0.246	0.0043	0.999	0.0043	32.31	
51	0.344	0.0060	0.999	0.0060	23.06	
53.6	0.246	0.0043	0.999	0.0043	32.31	
58.5	0.295	0.0052	0.999	0.0052	26.91	
62.8	0.295	0.0052	0.999	0.0052	26.91	